Imaging with two spiral diffracting elements intermediated by a pinhole

José J. Lunazzi,* Noemí I. R. Rivera, and Daniel S. F. Magalhães

Universidade Estadual de Campinas, Instituto de Física Gleb Wataghin, Caixa Postal 6165, 13083-970 Campinas, SP, Brazil
**Corresponding author: lunazzi@ifi.unicamp.br*

Received September 26, 2007; revised January 26, 2008; accepted January 29, 2008; posted March 4, 2008 (Doc. ID 87893); published April 21, 2008

A pseudoscopic (inverted depth) image made with spiral diffracting elements intermediated by a pinhole is explained by its symmetry properties. The whole process is made under common white light illumination and allows the projection of images. The analysis of this projection demonstrates that the images of two objects pointing away longitudinally have the main features of standard pseudoscopic image points. An orthoscopic (normal depth) image has also been obtained with the breaking of the symmetry conditions. © 2008 Optical Society of America

OCIS codes: 050.1970, 090.2870, 110.0110, 110.2990, 110.6880.

1. INTRODUCTION

Images obtained using three diffractive elements were studied and discussed theoretically by Sweatt [1], where it was proposed that the configuration could be used for a lightweight telescope when coupled with a converging lens. Weingärtner and Rosenbruch [2] used a system composed of a diffraction grating and a holographic lens to obtain an image of a far object. A photograph showed a sharp image at 10 nm bandwidth and a rough image when using the visible spectrum. To our knowledge no experimental result has been reported with a three-diffractive-element imaging system.

Lunazzi and Rivera [3–5] previously reported that the pseudoscopic image obtained with diffraction gratings intermediated by a slit converges only in the horizontal plane, thus generating an image which is not astigmatic for visual observation, but in which astigmatism precludes obtaining a convergent image. Reducing the slit to a pinhole eliminates astigmatism but reduces luminosity. Further work has shown [6,7] that convergence of all rays at the image position is obtained with the same geometry with bidimensionally structured diffracting elements and with the replacement of the slit by a pinhole. The chosen diffractive optical element (DOE) was a spiral one that could be considered equivalent to a circular one of constant period [8]. The element constitutes a diffractive axicon [9,10] making a succession of convergent beams along a resulting luminous line. This convergence restores luminosity to the image projection because it concentrates more light at the pinhole position. It was also reported [11] that an orthoscopic image can be obtained.

In this work, the above geometries are analyzed by ray tracing, and focusing experiments are performed. In Section 2 we present the basic formalisms required to describe pseudoscopic and orthoscopic images obtained with two diffracting elements intermediated by a pinhole. The experimental setup for focusing experiments is described in Section 3. Results and discussion are in Section 4 and conclusions in Section 5.

2. DESCRIPTION

A. Pseudoscopic Image

The diffracting elements we used to observe pseudoscopic images have the spiral groove format because digital data discs perfectly fulfill the requirements. The generation of nondiffracting beams by these elements was previously studied by Ferrari *et al.* [9].

Figure 1 shows the general view of the optical system used to obtain the pseudoscopic image of an object. To explain the imaging properties it suffices to consider that for each ray exiting from a point object, a plane can be selected to determine the image position, which is perfectly symmetric. With this geometry, the existence of light rays can be assured within an extensive region reached by the diffracted light after the first element. As can be seen in Fig. 1, circular symmetry extends the above properties to a family of planes within the whole volume defined by the selected experimental geometry.

We can choose one of these planes for the analysis. Figure 2 shows two object points A and B placed in front of the first diffraction element DOE1. The diffracted light from DOE1 passes through the pinhole P and reaches the identical diffraction element DOE2. In the present analysis the diffraction effects due to the pinhole itself are neglected. The dotted line in Fig. 2 gives the alignment of the DOE1 and DOE2 spiral centers with the pinhole P. It can be seen in this figure that with respect to the pinhole plane, the images A′ and B′ are symmetrical with A and B.

The whole space can thus be decomposed into a set of oblique planes containing the symmetry axis. The spreading of the diffracted beam that the first diffractive element generates ensures the existence a ray through the

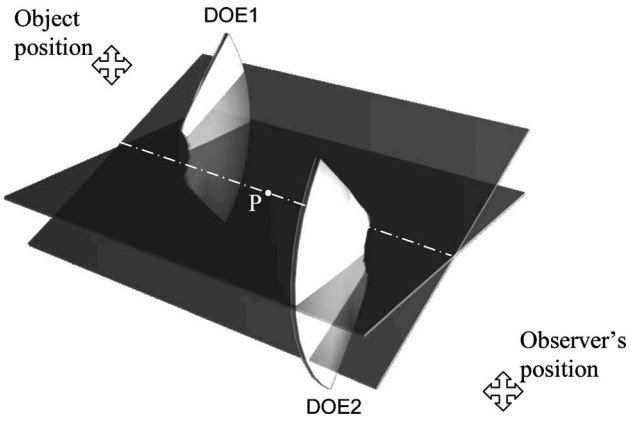

Fig. 1. General view of the optical system and the decomposing of the imaging process through a family of planes corresponding to circular symmetry.

pinhole P. The subsequent diffracted beam due to the second diffraction grating is directed toward the image point. The observer's position can receive rays from only one plane of the kind we selected, that of the plane where it is included. Rays not included in the selected planes undergo conical diffraction [12,13]. The reason rays spreading in different directions are present is that the observation of the whole image is possible from a single point of view. The observer sees the image of points at different planes because of the rays that are not on the planes we selected.

With this geometry, the observer sees a convergent image resulting from first and second diffractions on the same side as its own position, satisfying the general grating equation,

$$\sin\theta_i - \sin\theta_d = \frac{\lambda\nu}{\sin\phi}, \tag{1}$$

where θ_i represents the angle of incidence of light traveling from point A to the first diffracting element, θ_d represents the angle of diffraction for light that travels from points on the diffracting element to point P, ϕ is the angle a ray makes with the tangent to the grooves at the incidence point in case it goes out of the plane of Fig. 2. ν represents the inverse of the grating period, and a specific wavelength value λ is assigned to each ray. It suffices to characterize the image properties to consider ray tracing

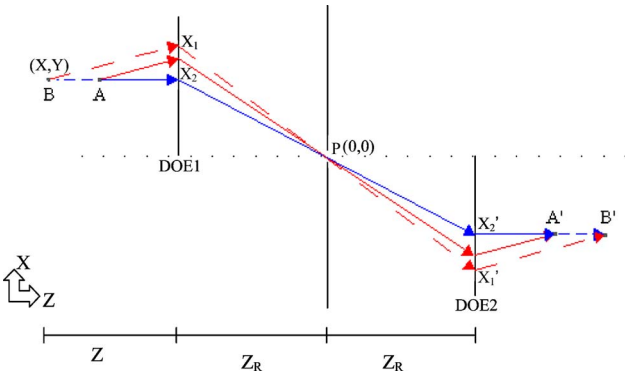

Fig. 2. (Color online) Image formation of two object points A and B.

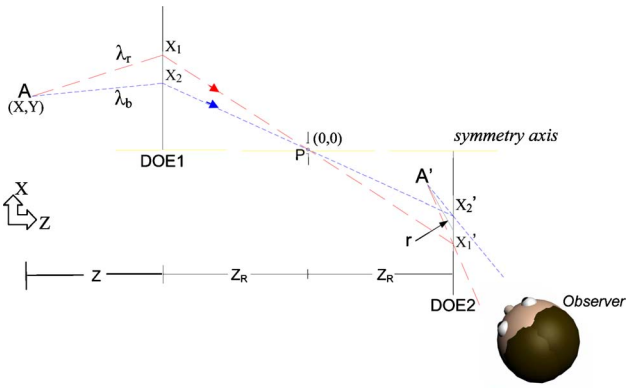

Fig. 3. (Color online) Ray tracing for the image of a point white-light object.

for rays with $\phi=90°$. All other rays converge to the same image point because of symmetry.

As can be expected for white light phenomena, extreme wavelength values are chosen to characterize the ray tracing; all other rays fall within these extremes. For each plane, the light path for the first diffraction can be represented by the set of Eqs. (2) and (3) below that describes the trajectories as if the gratings were straight-line gratings:

$$\frac{X_1 - X}{\sqrt{(X_1 - X)^2 + Z^2}} + \frac{X_1}{\sqrt{X_1^2 + Z_R^2}} = \lambda_v v,$$

$$\frac{X_2 - X}{\sqrt{(X_2 - X)^2 + Z^2}} + \frac{X_2}{\sqrt{X_2^2 + Z_R^2}} = \lambda_a v. \tag{2}$$

Path calculations obtained after the second diffraction are on the set of Eqs. (3), from which one obtains the position of an image point (X_i, Z_i) of an object point (X, Z):

$$\frac{X_1'}{\sqrt{X_1'^2 + Z_R^2}} + \frac{X_i - X_1'}{\sqrt{(X_i - X_1')^2 + Z_i^2}} = -\lambda_v v,$$

$$\frac{X_2'}{\sqrt{X_2'^2 + Z_R^2}} + \frac{X_i - X_2'}{\sqrt{(X_i - X_2')^2 + Z_i^2}} = -\lambda_a v. \tag{3}$$

In Eqs. (2) and (3), the ordinates X_1 and X_2 are points at the first grating where the paths for blue and red wave-

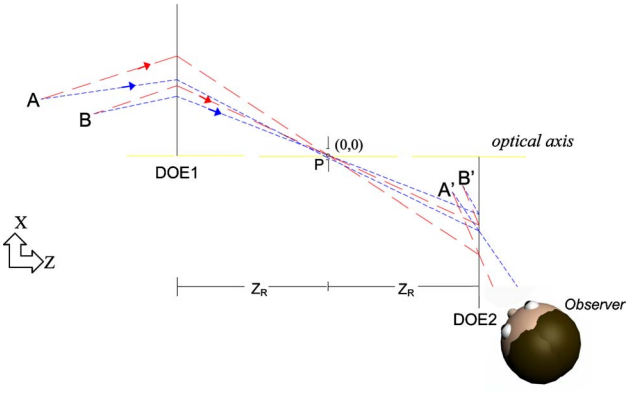

Fig. 4. (Color online) Ray-tracing scheme for the normal depth image.

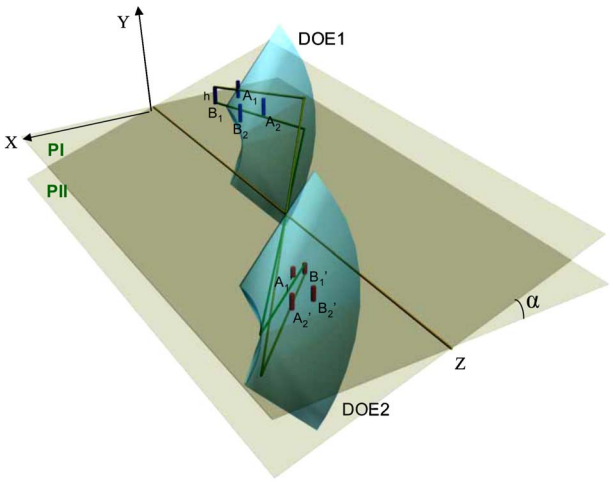

Fig. 5. (Color online) B_1' and B_2' are images of the objects B_1 and B_2, all of them belonging to planes PI and PII.

lengths are considered, respectively. Z and Z_R are the lengths between the object and DOE1 and between DOE1 and the pinhole, respectively (as shown in Fig. 2). The difference in the signal of the sin θ_d in Eq. (1) and the coordinates of Eqs. (2) and (3) follows the convention adopted by [14].

B. Orthoscopic Image

With the above described geometry, an orthoscopic image can be seen when flipping the second DOE and changing the angle for observation. The angle is changed to select the opposite diffraction order. It should be noted that the system geometry remains identical to that described above to obtain a pseudoscopic image. The ray scheme for this situation is shown in Fig. 3.

In Fig. 3, the white-light object A shines on the first of the two diffracting elements that are symmetrically located with respect to the pinhole P. The observer sees a diverging image resulting from these diffractions located between the pinhole and DOE2. As was the case in Subsection 2.A Eq. (2) is valid.

The paths at the second diffraction satisfy Eq. (4), differing only by a signal according to Eq. (3), from which one obtains the position of the image point:

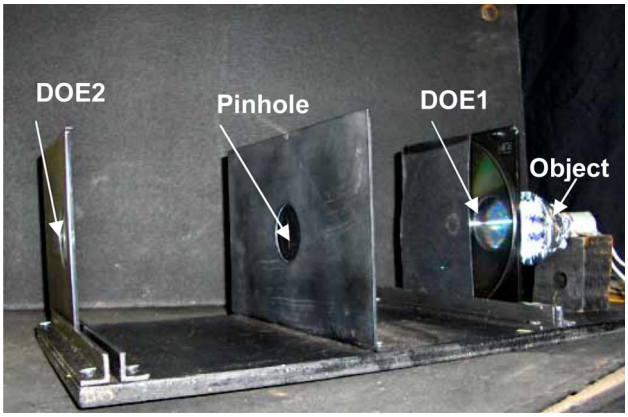

Fig. 6. (Color online) Experimental setup of a double diffraction system with a pinhole.

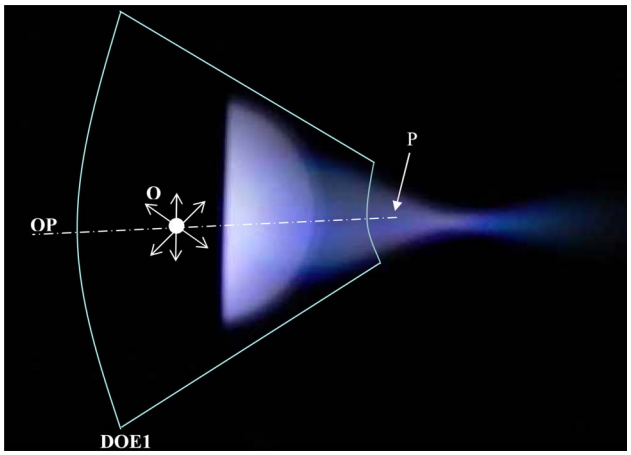

Fig. 7. (Color online) Light distribution reaching the pinhole P.

$$\frac{X_1'}{\sqrt{X_1'^2+Z_R^2}}+\frac{X_i-X_1'}{\sqrt{(X_i-X_1')^2+Z_i^2}}=\lambda_v v,$$

$$\frac{X_2'}{\sqrt{X_2'^2+Z_R^2}}+\frac{X_i-X_2'}{\sqrt{(X_i-X_2')^2+Z_i^2}}=\lambda_a v. \tag{4}$$

Figure 4 illustrates normal depth on the image for two object points A and B, located at different depth positions. As the figure shows, it was also verified that a shortening of the dimensions on the image happens in one direction along this plane. A left-to-right inversion is also a characteristic consequence of this image formation. Numerical calculations indicate that the image can be viewed binocularly, resembling a holographic image but with a spectral sequence of color change due to the wavelength changes associated with the displacements of the observer point of view.

The image features obtained in the present study with circular gratings are already present in the case of orthoscopic images obtained with ordinary straight-line gratings [5]. It is interesting to note that for both kinds of images, the diffracting elements can be any of a general variety: The major requirements are that the two diffractive elements be identical and that the second element be symmetrically oriented with respect to the line normal to the pinhole, satisfying the above described ray-tracing

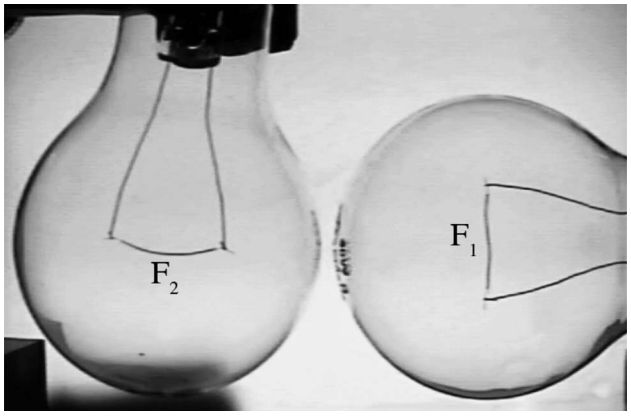

Fig. 8. Photos of the objects F_1 and F_2 used to obtain the pseudoscopic image.

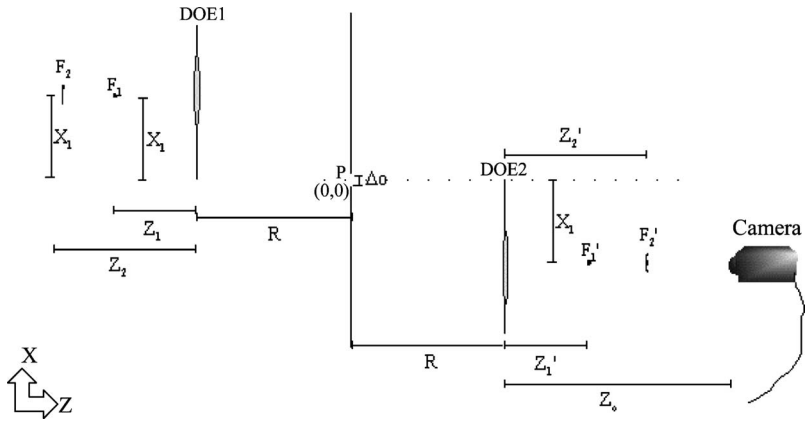

Fig. 9. Schematic view of the apparatus of image formation.

conditions. The more regular the element, the easier the alignment would be. A diffractive or holographic lens pair could bring more luminosity by concentrating the light at the pinhole region.

Rays outside our set of selected planes can reach the pinhole only through conical diffraction. The symmetry condition no longer applies, and this may be the cause of some aberration, an interesting case for further study.

In Fig. 5, there are four objects of height h in pairs at distances Z_1 and Z_2. The X coordinates of the objects named A or B are X_A and X_B, respectively. Two planes (PI and PII) are shown characterized because they are common to the symmetry axis and include the extremes of the objects B_1 and B_2. α is the angle between these planes, satisfying the relationship

$$\alpha = \arctan\left(\frac{h}{X}\right). \tag{5}$$

These planes determine the extension of the object B1 and also of its image B1′. Shown in the figure are the paths of two rays each exiting from the extremes of B1 until they reach its image.

The light path can be obtained from the following equations:

$$\frac{\dfrac{X_{1,2}}{\cos\alpha} - \sqrt{X^2+h^2}}{\sqrt{\left(\dfrac{X_{1,2}}{\cos\alpha} - \sqrt{X^2+h^2}\right)^2 + Z^2}} + \frac{\dfrac{X_{1,2}}{\cos\alpha}}{\sqrt{\left(\dfrac{X_{1,2}}{\cos\alpha}\right)^2 + Z_R^2}} = \lambda_{a,v} v, \tag{6}$$

$$\frac{-\dfrac{X_{1,2}}{\cos\alpha}}{\sqrt{\left(\dfrac{X_{1,2}}{\cos\alpha}\right)^2 + Z_R^2}} + \frac{\dfrac{X_{1,2}}{\cos\alpha} - X_i}{\sqrt{\left(\dfrac{X_{1,2}}{\cos\alpha} - X_i\right)^2 + Z_i^2}} = \lambda_{a,v} v. \tag{7}$$

Table 1. Experimental Checking of the Pseudoscopic Image[a]

R	Z_o	Δo	X_1	Z_1	Z_2	Z_1'	Z_2'
130±1	477±1	0.5±0.1	35±1	73±2	122±2	67±3	117±3

[a]All data in mm.

The extension of the image B′ is given by

$$h' = X_i \sin\alpha, \tag{8}$$

where X_i is determined by the system of Eqs. (6) and (7). These equations are necessary to completely describe the imaging process.

3. EXPERIMENTAL SETUP

The experimental system is shown in Fig. 6. The spiral transmission gratings DOE1 and DOE2 are two pieces of a compact disk with spatial frequency of 658±5 lines/mm at any radial distance, generating phase diffraction in the first order with 10.5% efficiency. The elements used in this study were originally transmissive in order to reduce the influence of surface distortion, but a reflective element can often be made transmissive by removing its reflective coating.

The objects employed have high brilliance to facilitate their location and for easily registering images. These objects were filament lamps with transparent bulbs, halogen or ordinary tungsten. A video camera SONY HANDYCAM CCD-TRV57 with adjustable focus, linked through a webcam Intel CS430 acting exclusively as a capture device, was employed for registering the images on a computer.

Figure 7 is a photograph showing the light distribution generated by the white point object O (a white-light LED) diffracted at DOE1 and reaching a region around the pinhole P. This region of diffracted light is 14 cm wide but only 4.5 cm in depth, corresponding to the first diffraction order selected in the present study. The dashed line identified as OP in Fig. 7 corresponds to the plane previously described in Fig. 2 on which the rays can pass the pinhole P for the subsequent formation of the image.

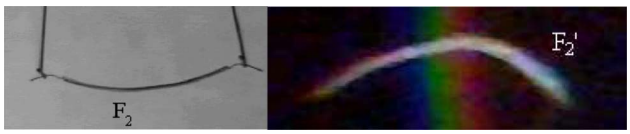

Fig. 10. (Color online) F_2 at left; image of F_2 (F_2') at right. The defocus of the image of F_1 is visible.

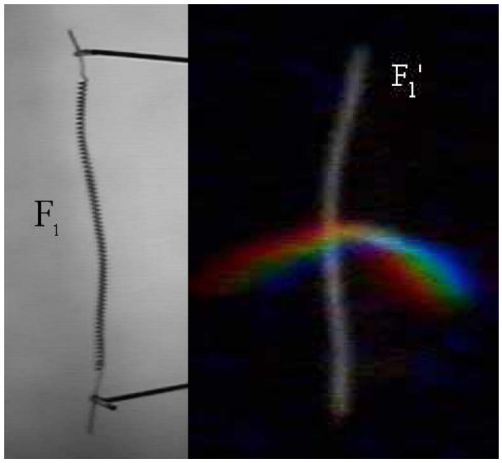

Fig. 11. (Color online) F_1 at left; image of F_1 (F_1') at right. The defocus of the image of F_2 is visible as a spectral dispersion.

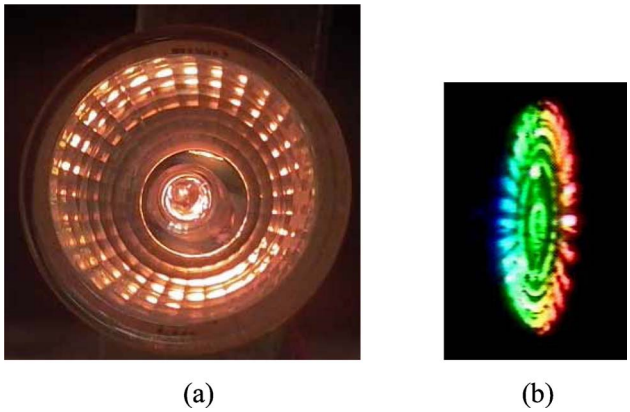

Fig. 12. (Color online) (a) Photograph of the halogen lamp employed as object. (b) Orthoscopic image of the object obtained in our system.

4. RESULTS AND DISCUSSION

A. Pseudoscopic Image

Figure 8 shows two tungsten filaments (F_1 and F_2) of 40 W lamps used as objects in this work. The filament directions are roughly orthogonal—F_1 positioned ahead of F_2—to the observer (camera) situated as shown in Fig. 9; this figure also gives an overall arrangement of the experimental setup. The values of the main ordinates and distances identified in Fig. 9 are given in Table 1. The image of the joint object constituted by the elements F_2' and F_1' is therefore pseudoscopic.

The focused images of each filament are shown in Figs. 10 and 11. It should be noted that these images are inverted in the vertical direction. The spectral dispersion crossing the filament image F_2' (Fig. 10, right) is due to rays that had composed F_1'. The defocused points appear with a chromatic spectrum whose width is proportional to the distance to the symmetry plane. The width of this dispersion retains the information of the depth of the image; this is known as "diffraction depth codification" [15,16].

Using binocular observations to study image depth properties is not possible in the pseudoscopic case because of the restricted angular extension of the image. If the present setup had binocular capability, an observer placed in the position Z_0 of the camera would have seen F_2' in front of F_1'. This is not the case in the present experiment.

In Table 1, one can see that $Z_2' \cong Z_2$ and $Z_1' \cong Z_1$, indicating that the symmetry proposed for the model geometry is experimentally fulfilled.

B. Orthoscopic Image

In the present experimental setup, the observation of orthoscopic images was done with a white-light object: a 20 W halogen lamp with parabolic reflector. This device provided observations of a very bright object, where a fraction of the diffracted light from the first element illuminates the region around the pinhole. Figure 12(a) shows a photograph of the object. Figure 12(b) shows the orthoscopic image obtained at an observer's distance $Z_c = (150 \pm 5)$ mm. This picture shows that the horizontal dimension appears reduced as compared with the vertical, which is in agreement with our ray-tracing analysis (Subsection 4.B.3 below). At object distances close to the first diffracting element this reduction is not noticeable—it appears only when the object is moved away.

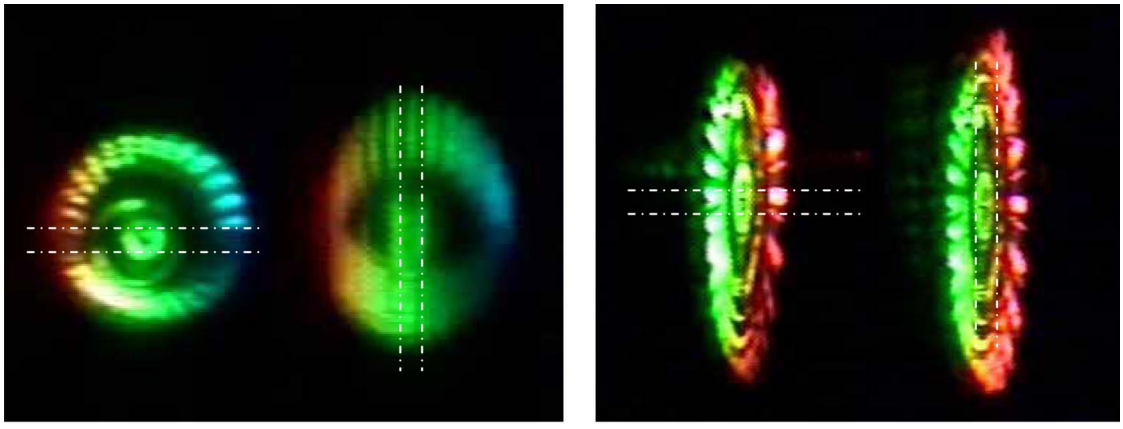

Fig. 13. (Color online) Dashed lines represent the slit position in (a) double-diffracted images for the plane grating case, (b) double-diffracted images for the circular grating case.

Table 2. Comparison between Experimental and Calculated Values of the Image Distance (mm)

Z	r_{exp}	r_{cal}
301±5	29±3	25±1
141±5	23±2	22±1
90±6	20±2	20±1
33±9	10±2	11±2

1. Astigmatism of the Image

The observed astigmatism is attenuated, if not eliminated, as compared with the case of a diffraction grating pair [5] because the chosen diffractive elements act in two dimensions thus forming a richer image. Figure 13(a) shows two images of the same halogen lamp obtained with ordinary straight gratings, while Fig. 13(b) corresponds to the case of the circular gratings. The images at the left in each part were obtained in both cases by covering the 32 mm diameter lens with a slit 1 mm thick oriented orthogonal to the (X,Z) plane. Correspondingly, in images at the right in each part, the slit was located parallel to the X direction. A comparison of Figs. 13(a) and 13(b) shows that the circular gratings provide a significant reduction in astigmatism.

2. Experimental Verification of the Image Position

In the present study, the numerical results of the model geometry were checked by measuring the image position with the focalization scale of a PENTAX-M reflex camera with an ASAHI 50 mm focal length objective. Different object positions were employed with the following input values: $\lambda_a = 500$ nm, $\lambda_v = 700$ nm, $Z_R = (126 \pm 4)$ mm, and $X = (37.0 \pm 0.5)$ mm. The numerical results shown in Table 2 were obtained with Eqs. (2) and (4), using the Mathematica 5.0 software by Wolfram Research.

3. Calculating the Horizontal and Vertical Extension of the Image

Horizontal Extension. In Fig. 5, the two object points A and B are shown with subscripts 1 or 2 indicating their different positions along the Z axis. Once again, Eqs. (2) and (4) were used to determine the horizontal extension $\Delta X_{i\mathrm{AB}}$ of the image A′, B′ with the input values $v = 658$ lines/mm, $\lambda_a = 400$ nm, $\lambda_v = 700$ nm, and $Z_R = 126.5$ mm. The calculated values of the horizontal image extension $\Delta X_{i\mathrm{AB}}$ are shown in Table 3.

The chosen values of $X_\mathrm{A} = 40$ mm and $X_\mathrm{B} = 30$ mm correspond to an object extension of $\Delta X_{\mathrm{AB}} = 10$ mm normal to the "optical axis" through the pinhole P.

Vertical Extension. To calculate the vertical extension h' [Eq. (8)] for two objects whose height is h located at positions $X_\mathrm{A} = 40$ mm and $X_\mathrm{B} = 30$ mm, the chosen input values were $v = 658$ lines/mm, $Z_R = 126.5$ mm, $\lambda_a = 400$ nm, and $\lambda_v = 700$ nm. The image extension h' was determined with Eqs. (6)–(8) using the software Mathematica 5.0. The derived results are shown in Table 4. The lengths on the drawing shown in Fig. 5 preserve the scale of these results, i.e., they are drawn to exhibit the two cases of Table 4. In this figure, PI and PII identify the obligatory planes corresponding to the extremes of the object B.

Table 3. Calculated Values of the Horizontal Image Extension (mm)

$Z_\mathrm{A}=Z_\mathrm{B}$	$X_{i\mathrm{A}}$	$Z_{i\mathrm{A}}$	$X_{i\mathrm{B}}$	$Z_{i\mathrm{B}}$	$\Delta X_{i\mathrm{AB}}$
33	−34.5	7.61	25.9	9.5	8.6
90	−31.3	12.3	−24.4	14.7	6.9
141	−30.3	13.9	−24.5	16.2	5.8

Table 4. Vertical Extension of the Image (mm)

$Z_\mathrm{A}=Z_\mathrm{B}$	$X_{i\mathrm{A}}$	$Z_{i\mathrm{A}}$	$X_{i\mathrm{B}}$	$Z_{i\mathrm{B}}$	h'_A	h'_B
33	−35.6	7.4	−27.2	9.2	8.6	8.6
90	−32.2	12.0	−25.5	14.3	7.8	8.1
141	−31.0	13.6	−25.4	15.8	7.5	8.0

5. CONCLUSIONS

In the present work is demonstrated the feasibility of a new system capable of producing white-light pseudoscopic and orthoscopic diffractive images. Calculations and measurements were shown to be in agreement. The choice of bidimensionally structured diffraction elements makes this system capable of projecting images that are pseudoscopic. Compared with previously reported systems [4,5], the present one permits the observation without astigmatism. This is advantageous since the images can be observed or photographed through a large aperture. In x-ray optics distortionless images can be achieved no matter how large the bandwidth.

REFERENCES

1. W. C. Sweatt, "Achromatic triplet using holographic optical elements," Appl. Opt. **16**, 1390–1391 (1977).
2. I. Weingärtner and K.-J. Rosenbruch, "Chromatic correction of two- and three-element holographic imaging systems," Opt. Acta **29**, 519–529 (1982).
3. J. J. Lunazzi, "Holoprojection of images by a double diffraction process," presented at XIV Encontro Nacional de Física da Matéria Condensada, Caxambu–Minas Gerais, Brazil, May 7–11, 1991.
4. J. J. Lunazzi and N. I. R. Rivera, "Pseudoscopic imaging in a double diffraction process with a slit," Opt. Express **10**, 1368–1373 (2002).
5. J. J. Lunazzi and N. I. R. Rivera, "Pseudoscopic imaging in a double diffraction process with a slit: critical point properties," J. Opt. Soc. Am. A **23**, 1021–1026 (2006).
6. J. J. Lunazzi and D. S. F. Magalhães, "Diffractive imaging with bidimensional elements: first experimental results," in *Proceedings of XXVII Encontro Nacional de Física da Matéria Condensada*, Poços de Caldas, MG, Brasil (May 4–8, 2004), Vol. 1, pp. 127.
7. J. J. Lunazzi and D. S. F. Magalhães, "Pseudoscopic white-light imaging by means of two bi-dimensional diffracting elements and a pinhole," Proc. SPIE **5622**, 1463–1468 (2004).
8. D. S. F. Magalhães, "Estudo de imagens por dupla difração com seleção de luz branca e elementos definidos bidimensionalmente," M.Sc. thesis (Instituto de Física Gleb Wataghin, Universidade Estadual de Campinas, 2005), http: // www.ifi.unicamp.br/ccjdr/teses/apresentacao.php3?filename=IF419.
9. J. A. Ferrari, E. Garbusi, and E. M. Frins, "Generation of nondiffracting beams by spiral fields," Phys. Rev. E **67**, 036619 (2003).

10. J. J. Lunazzi and D. S. F. Magalhães, "Photographing by means of a diffractive axicon," http://arxiv.org/pdf/physics/0701234.
11. J. J. Lunazzi and N. I. R. Rivera, "Orthoscopic imaging in a double diffraction process with slit," in *Proceedings of XXVII Encontro Nacional de Física da Matéria Condensada*, Poços de Caldas, MG, Brasil (May 4–8, 2004), Vol. 1, pp. 344–344.
12. E. N. Hogert, M. A. Rebollo, and N. G. Gaggioli, "Alignment and/or tilting measurement by means of conical diffraction phenomena," Opt. Laser Technol. **23**, 341–344 (1991).
13. N. I. R. Rivera, "Imagem por dupla difracao com luz branca sem elementos intermediários," Ph.D. thesis (Instituto de Fisica Gleb Wataghin, Universidade Estadual de Campinas, 2007), http://webbif.ifi.unicamp.br/teses/apresentacao.php?filename=IF284.
14. M. C. Hutley, *Diffraction Gratings* (Academic, 1982), pp. 23–26.
15. J. J. Lunazzi, "3D photography by holography," Opt. Eng. (Bellingham) **29**, 9–14 (1990).
16. J. J. Lunazzi, "Holophotography with a diffraction grating," Opt. Eng. (Bellingham) **29**, 15–18 (1990).